Sulfur/Polyacrylonitrile-Based N-Terminated Graphene Nanoribbon Cathodes for Li-S Batteries

Pouya Partovi-Azar*

Institute of Chemistry, Martin-Luther-University Halle-Wittenberg, Von-Danckelmann-Platz 4, Halle (Saale) 06120, Germany

(Received 24 July 2022; revised 15 September 2022; accepted 28 September 2022; published 28 October 2022)

Conductive sulfur/carbon copolymers with a high reversible capacity are promising alternative cathode materials for lithium-sulfur batteries. Here, the focus is set on nitrogen-terminated zigzag graphene nanoribbons (N-GNRs) resembling intermediate product of electrospun polyacrylonitrile (PAN)-based carbon nanofibers. In particular, the possibility of combining strong nitrogen-sulfur interactions, which has been recently shown to lead to a shuttle-free discharge mechanism, and superior electrical conductivity of graphene nanoribbons is explored in S/N-GNR copolymers. Structural and electronic properties of S_x/N-GNR structures, $x = 1, \ldots, 8$, prior and during the discharge are studied using density-functional theory calculations along with *ab initio* molecular dynamics simulations. It is found that the GNR backbone assumes a rippled structures in all S/N-GNR structures considered here. The most favorable sulfur structures in S/N-GNR copolymers are found to consist of short sulfur chains with $x \sim 4, 5$. It is also observed that, similar to N-GNRs, S/N-GNR copolymers show a metallic behavior which is brought about by the conductive backbone. In addition, consecutive lithiation reactions are studied and product structures are obtained. It is demonstrated that a shuttle-free, solid-solid transformation could also be expected during the discharge of S/N-GNR copolymers, whereas the lithiated structures remain electrically conductive, irrespective of the discharge state. Therefore, the current study promotes the use of S/N-GNR copolymers as an alternative to other poorly conductive PAN-based S/C copolymer cathodes for lithium-sulfur batteries (such as S/cPAN), while largely mitigating lithium polysulfide formation.

DOI: 10.1103/PhysRevApplied.18.044072

I. INTRODUCTION

Lithium-sulfur (Li-S) batteries are considered to be among promising candidates for next-generation Li-based batteries and have been the subject of numerous experimental and theoretical studies in the past years [1–23]. However, Li-S batteries suffer from a irreversible capacity fade which arises from Li-polysulfide diffusion through the electrolyte during the discharge [1]. Sulfur/carbon copolymers have recently been shown to largely limit this process [23–25], mainly due to their structural flexibility which also helps the cathode material withstand the volume expansion at the fully discharge state of the battery. In particular, sulfur/carbon copolymers based on polyacrylonitrile (PAN) have attracted much attention as they appear to largely mitigate the shuttle effect during the discharge [26–34]. This desirable performance is mainly attributed to the formation of short sulfur chains along the active N-doped edges of the copolymer. This is believed to result in a solid-solid transformation of the cathode during the lithiation minimizing the shuttle effect to a great extent [34].

However, even for S/PAN compounds, a clear picture on the favorable edge structures (-N-S_x-N-) and their lithiation mechanism on an atomistic level is still not fully established. Moreover, the cathode materials should preferably be electrically conductive. In this regard, graphene nanoribbons with fully N-terminated edges (N-GNRs) could provide a more desirable cathode material, benefiting from both a similar active edge structure as well as the superior conductivity of graphene nanoribbons [35,36]. N-GNRs can form during the synthesis of PAN-based carbon nanofibers, for example, through electrospinning method. They usually emerge in the carbonization process while their widths can be controlled through sequential denitrogenation at high temperatures (above 1500 °C) [37,38]. It has been shown that narrow N-GNRs show finite magnetic moment whereas the wider N-GNRs are nonmagnetic [39]. N-GNRs could be considered as local structural elements in PAN-based carbon nanofibers, which due to their stability, high electrical conductivity, and the possibility of functionalization, have been used in many energy-related applications, such as supercapacitors [40] and Li-ion batteries [41,42].

In this article, using density-functional theory (DFT) calculations the most favorable sulfur structures on fully

*pouya.partovi-azar@chemie.uni-halle.de

nitrogen-doped edges of S_x/N-GNR copolymers are studied. In particular, the possibility of formation of a wide range of sulfur structures on the edge, namely those consisting of sulfur radicals, sulfur chains with varying number of sulfur atoms ($1 \leq x \leq 8$), and chains with different distances between the terminal sulfur atoms connecting the chain to the GNR backbone are explored. In addition, the effect of sulfur structures on the electronic properties of the S_x/N-GNR polymers is investigated. Finally, we complement our investigations by studying the lithiation of S/N-GNR copolymer cathodes during the discharge.

II. METHODOLOGY

Here, N-GNRs with five rings across are considered (Fig. 1). Although the magnetic ordering in narrower N-GNRs has already been shown to be fragile, an N-GNR with five rings across has been reported to be the narrowest nonmagnetic ribbon [39]. The reaction of sulfur atoms with the N-GNR is only studied (otherwise stated) on one edge of the ribbon and similar reactions with the other N-doped edge are assumed to yield similar product structures. In particular, the following reaction is considered

$$\left(\frac{x}{8}\right) S_8 + \text{N-GNR} \longrightarrow S_x/\text{N-GNR}, \qquad (1)$$

where $x = 1, \ldots, 8$. In this hypothetical reaction we also assume that an infinitely large reservoir of S_8 molecules with zero chemical potential is available. The ribbon is assumed to lie along the z axis on the xz plane. A periodic supercell along the ribbon axis with 10 repetitions of the N-GNR unit cell along the z axis is considered (Fig. 1). As such, the initial unit cell for all the samples has a 30.00 Å × 20.00 Å × 24.60 Å size. The unit cell vectors along x and y axes are chosen long enough to avoid interaction with the periodic replicas. In all cases, the atomic coordinates as well as the unit cell vector along the z axis are optimized, while keeping the other unit cell vectors fixed. The external pressure is to 0.0 GPa while the pressure tolerance and maximum atomic force component are set to 0.01 GPa and 0.02 eV/Å, respectively. The full geometry optimization is first performed for N-GNR without sulfur atoms and then the optimized cell is used as a starting cell for the full optimization of S/N-GNR systems.

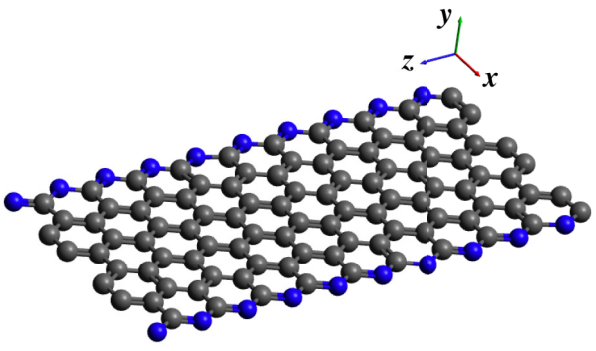

FIG. 1. Structure of a periodic supercell for an N-GNR considered in this work. Gray and blue spheres denote N and C atoms.

Calculations are performed at DFT level mostly using the CP2K software [43]. A double zeta plus polarization basis function optimized for molecular systems (DZVP-MOLOPT) [44] along with Geodecker-Teter-Hutter (GTH) pseudopotentials are used [45]. The exchange and correlation effects are approximated using Perdew-Burke-Ernzerhof (PBE) functional [46] together with DFT-D3 method [47] which accounts for long-range dispersion interactions. For a better structural sampling of S_x/N-GNR ($2 \leq x \leq 8$) systems involving sulfur chains, *ab initio* molecular dynamics (AIMD) simulations are also performed. These simulations are performed using CP2K software in canonical ensemble at 300 K, where the temperature is controlled by a canonical sampling through velocity rescaling (CSVR) thermostat [48]. The time step is set to 1.0 fs and the total equilibration time is 50 ps.

Electronic properties of S/N-GNR structures before and after lithiation reactions are calculated using the SIESTA code [49] with pseudoatomic orbital basis functions along with norm-conserving Troullier-Martins-type pseudopotentials [50]. The Monkhorst-Pack k grid [51] is set to $1 \times 1 \times 15$, and a real-space mesh cutoff of 350 Ry is used. In these calculations, again the PBE approximation is used for the exchange and correlation effects. Prior to electronic structure calculations, all optimized structures obtained through CP2K calculations are fully optimized (unit cell together with atomic coordinates) again using SIESTA with the same optimization criteria.

III. RESULTS AND DISCUSSION

A. Structural properties

For each x, first we energetically compare the structures where sulfur atoms form a single chain, multiple chains, and conformations which involve sulfur radicals. The results for $x = 2, 3$, and 4 are shown in Fig. 2. From Figs. 2(a) and 2(b), it can be concluded that, as expected, formation of sulfur radicals in S_x/N-GNR structures (shown as red data points) are thermodynamically less favorable. Moreover, as shown in Fig. 2(c), multiple sulfur chains along the N-GNR are also less likely to form.

Therefore, hereafter only those S_x/N-GNR structures are considered for $2 \leq x \leq 8$ where the sulfur atoms form one single chain along the N-GNR. In order to find the most favorable conformations, the following procedure is adapted: in a first step, full structural optimization (unit cells together with atomic coordinates) is performed at zero temperature. In each case (except for $x = 2$), the distance between the terminal sulfurs are changed in order to find

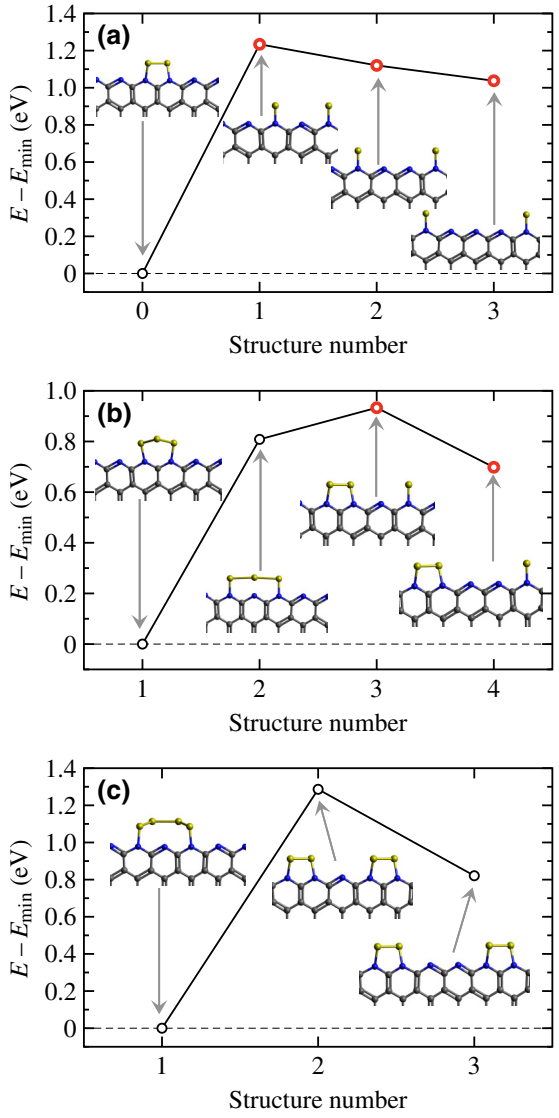

FIG. 2. Total energies (referenced to the minimum value in each case) for (a) $x = 2$, (b) $x = 3$, and (c) $x = 4$. The data points corresponding to structures involving sulfur radicals are shown in red.

the most favorable atomic configuration. Figure 3 shows the energies for S_x/N-GNR systems with $3 \leq x \leq 8$ as a function of distance between the terminal sulfur atoms. The distance, d, is given in terms of the number of carbon rings between the terminal sulfur atoms. For $x = 3$, the favorable structure is the one where $d = 1$, whereas for $x = 4, 5$, and 6, $d = 2$ is the favorable distance between the terminal S atoms. For $x = 7$ and 8, the favorable distance between the terminal S atoms is $d = 3$. At the end of this geometry optimization step, all the atomic structures are found to consist of a planar N-GNR.

In a second step, AIMD simulations are performed on the lowest-energy structures in Fig. 3 for $3 \leq x \leq 8$ (shown in red) as well as on sulfur-free N-GNR in order to improve the sampling of the configuration space. The AIMD simulations are performed at 300 K in canonical ensemble for 50 ps starting from the respective optimized unit cells and atomic coordinates. Typical graphene-like corrugations are observed in all samples at 300 K [52–55]. The ripples are found to be stationary with respect to typical timescales attributed to honeycomb lattice vibrations. Furthermore, the effect of basis set quality on the observed structural properties is explicitly inspected using a larger basis set. Similar characteristic ripples are also observed with a triple-ζ basis set.

In a final step, from these rippled structures another round of full geometry optimizations is performed. It is found that the rippled structures are more energetically favorable in all cases. In the optimized structures, the unit cell vector along the N-GNR axis, $\mathbf{a}_3$, is found to be typically around 0.65 Å shorter than the respective unit cell vector obtained in strictly planar backbones at $T = 0$ K. Figure 4(a) shows the length of the unit cell vector, $\mathbf{a}_3$, along the ribbon axis as a function of x. Figure 4(b) shows the optimized structures for the N-GNR, S_4/N-GNR, and S_8/N-GNR samples. We observe that a rippled configuration is more favorable, even in the case of N-GNR. This finding hints at nitrogen atoms being the main cause for the rippled structures rather than the S chains. The structure optimization is also done on a longer N-GNR sample with 20 repetitions of the ribbon unit cell along the z axis [Fig. 4(c)]. Similar corrugations with a wave length of around 23 Åare observed. The average amplitude of the ripples is found to be 1.75 Å.

The optimized structures obtained through the procedure described above are then used to calculate the respective

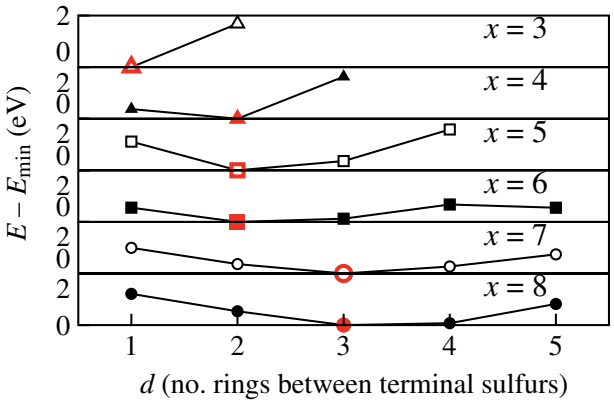

FIG. 3. Total energies (referenced to the minimum value in each case) for $x = 3, \ldots, 8$.The data points shown in red correspond to the minimum-energy structures which are used for AIMD simulations in the second step of full structural optimizations (see the text).

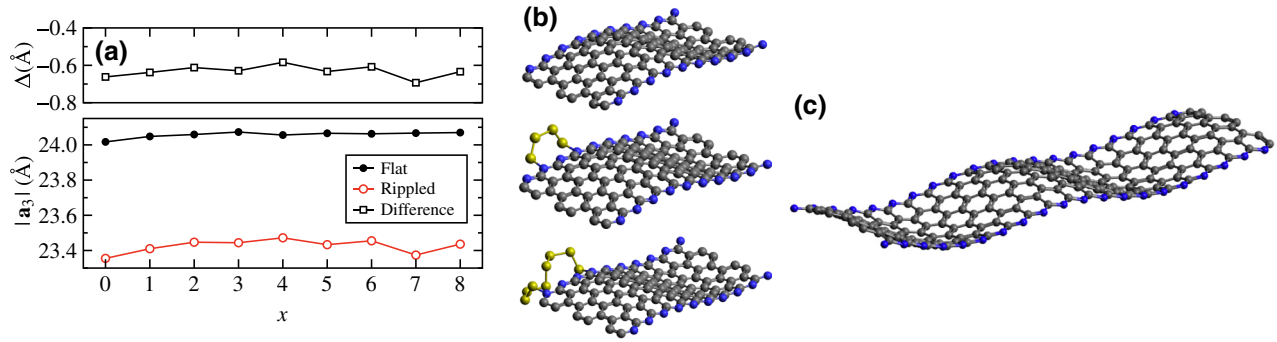

FIG. 4. (a) Length of the unit cell vector along the ribbon axis, $|\mathbf{a}_3|$, in S_x/N-GNR systems as a function of x, obtained after the final step of structure optimization (hollow red circles; see the text). Black solid circles show the same after the first step of optimization. Hollow black rectangles denote the difference. (b) Optimized structures of the N-GNR, S_4/N-GNR, and S_8/N-GNR samples obtained after the final step of optimization. (c) Optimized structure of a long N-GNR sample with 20 repetitions of the ribbon unit cell along the z axis.

formation energies based on reaction (1) as

$$E_{\text{form}} = \frac{1}{x}\left[E_{S_x/\text{N-GNR}} - E_{\text{N-GNR}} - \left(\frac{x}{8}\right)E_{S_8}\right], \quad (2)$$

where $E_{S_x/\text{N-GNR}}$, $E_{\text{N-GNR}}$, and E_{S_8} are the total DFT energies of the S_x/N-GNR samples, a pristine (sulfur-free) N-GNR, and an S_8 ring, respectively. The results are shown in Fig. 5(a). Figure 5(b) shows the probabilities of formation calculated according to

$$p_x = \frac{e^{-E_x^{\text{form}}/k_BT}}{\sum_x e^{-E_x^{\text{form}}/k_BT}}, \quad (3)$$

where k_B is the Boltzmann constant and $T = 300$ K. It is found that short S_x chains ($x = 4, 5$) are more likely to form on the N-GNR edges. This finding is in agreement with recent reports on the structure of several sulfur/carbon copolymers [25,56]. According to these results, with S/N-GNR polymers as a cathode material for Li-S batteries, the formation of higher Li-polysulfides (Li_2S_x, $6 \leq x \leq 8$), which are more soluble in commonly used electrolytes, could be largely avoided. These findings are promising because the problem of poor cyclability due to the diffusion of higher Li-polysulfides from the cathode into the electrolyte could be mitigated using S/N-GNR cathodes. However, polymeric sulfur cathodes might, in general, provide a lower maximum voltage compared with, for example, cathodes based on bulk orthorhombic sulfur, due to the fact that shorter S chains are more favorable in these systems. Based on the formation probabilities of S chains [Fig. 5(b)], it is possible to estimate sulfur wight percentage in S/N-GNR structures where multiple S chains are attached along the two edges. Our calculations show that in order for the S chains to form multiple stable chains along an edge, they should be at least two carbon rings apart from each other. As such, the maximum weight percentage of sulfur in an S/N-GNR copolymer with five rings across is calculated to be around 35%.

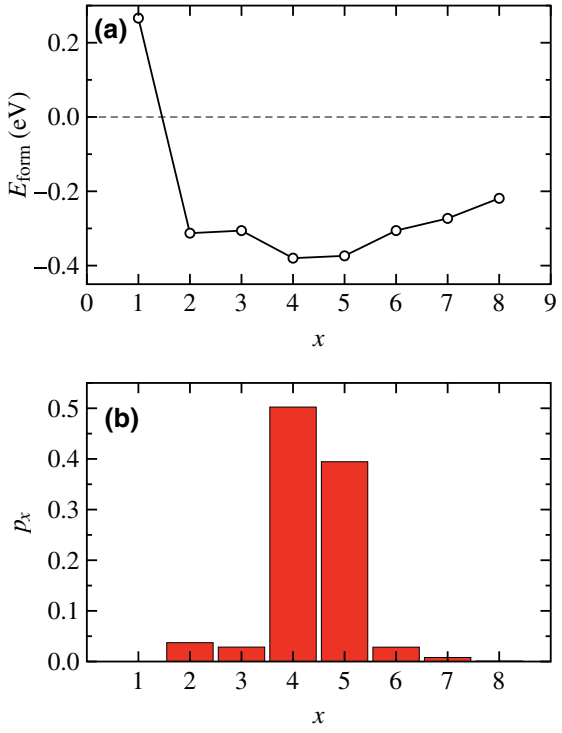

FIG. 5. (a) Formation energy and (b) formation probability of S_x/N-GNR systems as a function of x.

Finally, another round of AIMD simulations are performed on S_4/N-GNR and S_8/N-GNR as prototypical S/N-GNR copolymer structures for 50 ps in canonical ensemble at 300 K starting from the optimized structures found through the procedure described previously. It is observed that not only the corrugated N-GNR backbone

remains intact in these structures, but the relative positions of S atoms with respect to the other sulfur atoms and the backbone also remain virtually unchanged.

As far as the structural properties are concerned, our specific inspection based on the same minimum-energy-configuration search described previously reveals that GNRs, unlike N-GNRs, do not assume a corrugated structure in their minimum-energy conformation. Moreover, what makes N-GNR a promising alternative cathode for Li-S batteries has to do with the fully N-doped edges, which provide highly reactive sites for reaction with sulfur. This property is absent in GNRs, which normally show hydrogen saturation along both edges. The hydrogen saturation makes it energetically unfavorable for sulfur chains to form chemical bonds with the GNR, because the process would inevitably involve breaking of H-C bonds [57].

B. Electronic properties

The electronic properties of S_x/N-GNR structures are investigated in terms of electronic density of states close to Fermi level. Figure 6(a) shows the total density of states for N-GNR, S_5/N-GNR, S_8/N-GNR, and $2S_4$/N-GNR/$2S_4$ systems. In the latter system two S_4 chains are connected to each N-doped edge of GNR backbone (a total of four S chains in the unit cell), and is considered to explicitly inspect the effect of more S content. The weight percentage of sulfur in this structure is about 30%. Despite their rippled structures and irrespective of their S content, all samples are found to remain metallic. However, compared with N-GNR, the density of states at the Fermi level decreases substantially when sulfur chains are present. Considering S_5/N-GNR and S_8/N-GNR systems, it is observed that the chain length does not appear to have a significant effect on the density of states at the Fermi energy.

As shown in Fig. 6(b), the finite density of states at the Fermi level in N-GNR, S_5/N-GNR, S_8/N-GNR (not shown) structures, arises from nearly identical contributions of N and C atoms. This has been reported before in the case of pristine (undoped) N-GNRs [39]. However, the finite density of state at the Fermi level is found to arise solely from carbon atoms in $2S_4$/N-GNR/$2S_4$. Moreover, although the contribution of S atoms in -1.0 eV $\leq E \leq 1.0$ eV to the total density of states is almost negligible in S_5/N-GNR and S_8/N-GNR systems, their contribution becomes more profound in $2S_4$/N-GNR/$2S_4$ at $\sim$450 meV [top panel of Fig. 6(b)] and seems to represent a localized state.

C. Lithiation products

Lithiation reactions are studied for S_4/N-GNR sample which is found to have the lowest formation energy (Fig. 5). The aim is to gather information on possible product structures during the discharge. Therefore, only the thermodynamics of lithiation reactions are studied here.

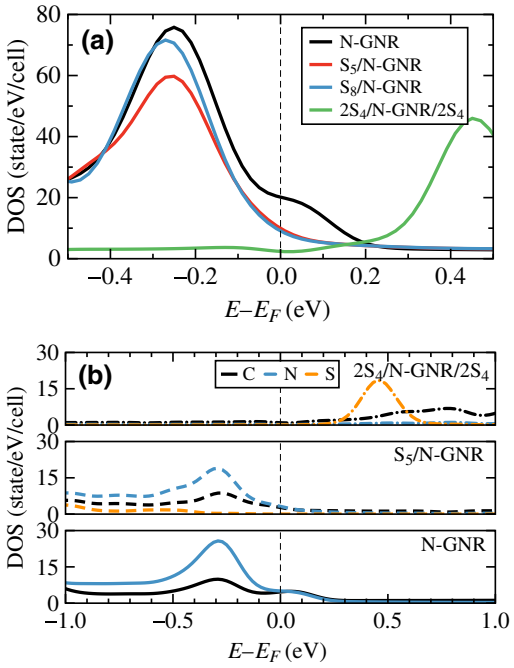

FIG. 6. (a) Total and (b) projected density of electronic states close to Fermi level.

The sample is sequentially lithiated until the maximum lithium capacity of sulfur is reached, namely two Li per S. For this, eight reactions are studied where a single lithium atom reacts with the sulfur cathode at each step according to the reaction

$$\mathrm{Li}_n\mathrm{S}_4/\text{N-GNR} + \mathrm{Li}^+ + 2e^- \rightarrow \mathrm{Li}_{(n+1)}\mathrm{S}_4/\text{N-GNR}, \quad (4)$$

where $n = 0, \ldots, 7$. In addition, the intermediate reactions, namely the oxidation of Li at the anode and possible reduction of S_4/N-GNR at the cathode are neglected. As such, reaction (4) corresponds to the overall cathode reaction.

The reactant structure in the first lithiation reaction is obtained by exploring the enthalpy landscape of a system in which a lithium atom is positioned around the sulfur chain of S_4/N-GNR. For this, 17 distinct positions are considered [57]. The reactant structure with the lowest energy is shown in the top panel of Fig. 7(a) in which the Li atom attacks a side S-S bond. It is worth noting here that, despite a nearly symmetric structure of the S_4 chain, the side S-S bonds are nonidentical due to the rippled structure of the N-GNR backbone. This results in reactant structures with slightly different energies when a lithium atom attacks each side S-S bond. Through geometry optimizations (no further unit cell optimization is performed), it is found that the product structure after the first lithiation reaction corresponds to the one in which the Li atom is positioned between two nitrogen atoms on the edge of N-GNR [lower panel of Fig. 7(a)].

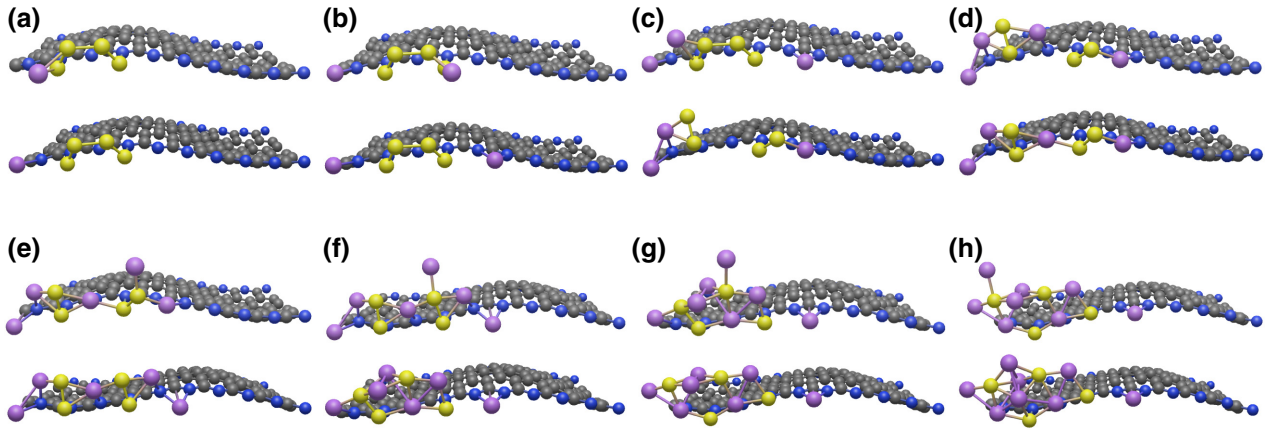

FIG. 7. Computed reactant (top panels) and product (bottom panels) structures corresponding to consecutive lithiation reactions of S_4/N-GNR sample according to reaction (4).

To study the second lithiation reaction, again 17 initial structures are considered where a second lithium atom reacts with the lithiated structure shown in the lower panel of Fig. 7(a). The enthalpy landscape is explored through the same process mentioned previously. The reactant structure with the lowest energy is shown in the top panel of Fig. 7(b) in which the Li atom attacks the other side S-S bond. Similar to the first reaction, thermodynamically favorable product structure is again found to be that in which the Li atom is positioned between two edge nitrogens on the other side of S_4 chain [lower panel of Fig. 7(b)].

Initial structures for the third lithiation reaction are prepared as described previously. The reactant structure with the lowest energy is presented in the upper panel of Fig. 7(c). This configuration corresponds to a structure where the additional lithium atom approaches a side S-S bond. This results in breaking of the central S-S bond and the side S-S bond being rotated towards the Li atoms to the left and right [lower panel of Fig. 7(c)].

For the fourth reaction, 10 distinct initial structures are considered. The lowest-energy structure corresponds to that shown in the upper panel of Fig. 7(d) in which a fourth Li atom is positioned between the two side S-S bonds. Optimization of this structure results in a comparable product structure where the new Li atom forms a covalent bond with an edge nitrogen and remains at an equal distance of about 2.5 Å from three S atoms [lower panel of Fig. 7(d)].

The lowest-energy reactant structure for the fifth lithiation reaction and the corresponding product structure obtained after geometry optimization are shown in the top and bottom panels of Fig. 7(e), respectively. In the fifth, sixth, seventh, and eighth lithiation reactions a similar pattern is observed: the reactant structures with the lowest energy in these reactions correspond to one in which the added Li atom approaches the Li-S cluster along the direction perpendicular to the N-GNR. The product structure after the fifth lithiation reaction also represents an almost symmetric structure along the ribbon edge. In addition, it is observed that at the fifth step the N-GNR backbone also undergoes a structural change upon lithiation which lowers the total energy of the system by about 320 meV. This could be related to the fact that the curvature-induced overlap between the π electrons in a graphene-based structure could be more in the valleys of the structure than that on the hills. The same effect has been shown to result in charge inhomogeneity on intrinsically rippled graphene samples [54,55]. Here, it appears that the accumulation of lithium around the sulfur content forces the N-GNR backbone to assume a valley-shaped structure close to lithium atoms where the stronger electrostatic interaction between the Li atoms and the N-GNR π electrons lowers the total energy. During subsequent lithiation steps, N-GNR retains its new configuration which further supports the above argument.

The lowest-energy reactant structure of the sixth lithiation and the obtained product structure are shown in the top and bottom panel of Fig. 7(f), respectively. This represents the first lithiation reaction which results in breaking of a side S-S bonds (the S-S bond on the right). Moreover, It is observed that the side lithium pairs formed after the fifth lithiation reactions are transferred back to form a similar connection with the edge nitrogens in steps 1 and 2 [Figs. 7(a) and 7(b)].

As shown in the lower panel of Fig. 7(g), breaking of the other side S-S bond (left) occurs in the seventh lithiation reaction.

Similar to the reactant structure in the previous steps, the final reactant structure is found to consist of a lithium atom approaching a sulfur atom along the perpendicular direction [upper panel of Fig. 7(h)]. As shown in the lower panel, the product structure is formed through a small structural change, in which the added lithium atom is transferred to the top of the nearby local Li_2S_2 structure [lower panel of Fig. 7(h)].

To make sure that all product structures represent stable configurations, AIMD simulations in the canonical ensemble are performed on each structure at 300 K for 10 ps. It is found that apart from thermal fluctuations in atomic positions, all product structures reported previously retain their overall zero-temperature configuration whereas the rippled structure of the N-GNR remains virtually intact.

According to these results, the formation of soluble Li-polysulfides appears to be unlikely due to strong N-S bonds. In fact, our calculations show a strong binding between the N-GNR backbone and the Li_nS_4 structures. The binding energies are calculated as $E_{\text{bind}} = E_{Li_nS_4/\text{N-GNR}} - E_{Li_nS_4} - E_{\text{N-GNR}}$, considering the product configurations shown in Fig. 7 [57]. The binding energies are all corrected for the basis set superposition error using the counterpoise correction [58]. In particular, for $n \geq 2$, the binding energies are more than twice as high as a typical N-S single covalent bond energy, namely approximately 4.8 eV [59], which emphasizes the important role of the Li ions in stabilization of lithiated S/N-GNR structures. This would then suggest that the overall interaction between the Li-S structures and the N-GNR backbone could be partially ionic. Therefore, a similar solid-solid transition during the discharge previously reported in S/cPAN copolymers could be expected in S/N-GNR copolymers as well. Moreover, similar to the case of S/cPAN [34], a single-plateau voltage versus depth of discharge curve is observed here (Fig. 8). The average cell voltage is calculated using

$$V = \frac{-\Delta G}{zF}, \tag{5}$$

where ΔG is the Gibbs free energy of each lithiation in reaction (4), z is the transferred charge, and F is the Faraday constant. Here, neglecting the entropic contributions to the Gibbs free energy, we approximate ΔG with the difference in the total DFT energies of products and reactants at each lithiation step.

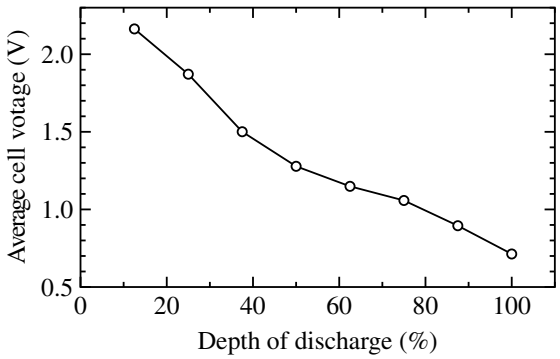

FIG. 8. Average cell voltage as a function of depth of discharge corresponding to the lithiation reactions in Fig. 7.

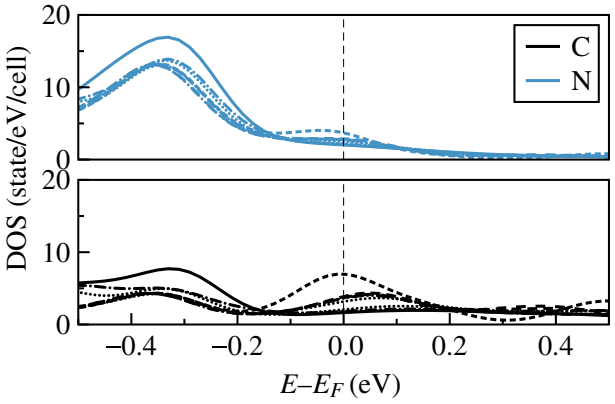

FIG. 9. Projected density of electronic states for carbon and nitrogen atoms in product structures Li_nS_4/N-GNR ($n = 1, \ldots, 8$) shown in black and blue curves, respectively.

Comparable -N-S_x-N- groups at the fully charged state of the cathode as well as a gradual S-S bond breaking during the discharge are also found here in S/N-GNR copolymers. However, unlike S/cPAN copolymers, no clear evidence for N-S bond breaking is observed in S/N-GNR structures during the discharge, and therefore, formation of free Li_2S molecules cannot be expected here. Such differences could be related to the fact that although the formation of similar -N-S_x-N- groups are observed in both S/cPAN and S/N-GNR copolymers, the local structures around S chains are considerably different in two systems, due to dissimilar backbone structures. This could, in turn, bring about substantially dissimilar electronic charge distribution around the S chains which could result in different N-S bond strengths. In fact, the binding energy between the S_4 chain and the backbone is calculated to be about 1.7 times higher in S_4/N-GNR compared to S_4/cPAN.

All lithiated structures are also found to remain electrically conductive irrespective of lithium content. Similar to the case of nonlithiated S/N-GNR copolymers, the metallic behavior in the lithiated structures is found to arise from carbon backbone as well as the nitrogen-doped edges (Fig. 9). It is also observed that in the early lithiation steps of S/N-GNR copolymers, the product structures could become magnetic [57]. The spin ordering along two edges have been reported in H-terminated and nitrogen-doped graphene nanoribbons before and has been shown to be energetically more favorable than a nonmagnetic electronic ground state [39,60].

IV. CONCLUSIONS

Sulfurized polyacrylonitrile (S/cPAN), as a cathode material for lithium-sulfur batteries, has been recently reported to show an intrinsic shuttle-free capability during cycling with a high reversible capacity. This capability has been mostly attributed to the formation of -N-S_x-N-

bridges stabilized through strong N-S bonds. However, S/cPAN suffers from poor electrical conductivity demanding the use of additional conductive carbon material. Sulfurized N-terminated graphene nanoribbons (S/N-GNRs), not only provide the same bonding between S and N atoms, but have also been demonstrated to have metallic properties. Here, the possibility of using S/N-GNR copolymers as cathode materials for lithium-sulfur batteries is explored. To this end, quantum-chemical calculations are performed to study the structural and electronic properties of S/N-GNR systems examining the formation of different sulfur structures. It is revealed that sulfur structures in the form of short S chains are thermodynamically more favorable. In addition, the product structures during the consecutive reactions with lithium are investigated. It is found that the N-GNR backbone assumes a rippled structure irrespective of sulfur and lithium content. Therefore, the rippled atomic configuration appears to be a result of the fully N-doped edges of N-GNR. It is also observed that, similar to S/cPAN, a solid-solid transformation could be expected in S/N-GNR copolymers upon lithiation, due to strong binding of lithium-sulfur structure to the N-GNR edge. Furthermore, it is shown that the S/N-GNR copolymers remain metallic throughout the discharge, suggesting a better performance as a cathode compared to S/cPAN.

ACKNOWLEDGMENTS

The author thanks Daniel Sebastiani for his support and fruitful discussions. The author also gratefully acknowledges DFG funding via projects PA3141/3 (Project number 420536636) and PA3141/5 (Project number 446879138). The computations have been performed on a Bull Cluster at the Center for Information Services and High Performance Computing (ZIH) at TU Dresden via the project 'p_oligothiophenes'.

[1] M. A. Weret, W.-N. Su, and B. J. Hwang, Strategies towards high performance lithium-sulfur batteries, Batteries Supercaps **5**, e202200059 (2022).
[2] M. Zhao, B.-Q. Li, X.-Q. Zhang, J.-Q. Huang, and Q. Zhang, A perspective toward practical lithium–sulfur batteries, ACS Cent. Sci. **6**, 1095 (2020).
[3] Y. Chen, T. Wang, H. Tian, D. Su, Q. Zhang, and G. Wang, Advances in lithium–sulfur batteries: from academic research to commercial viability, Adv. Mater. **33**, 2003666 (2021).
[4] L. Huang, J. Li, B. Liu, Y. Li, S. Shen, S. Deng, C. Lu, W. Zhang, Y. Xia, and G. Pan, *et al.*, Electrode design for lithium–sulfur batteries: problems and solutions, Adv. Funct. Mater. **30**, 1910375 (2020).
[5] S. Huang, Z. Wang, Y. Von Lim, Y. Wang, Y. Li, D. Zhang, and H. Y. Yang, Recent advances in heterostructure engineering for lithium–sulfur batteries, Adv. Energy Mater. **11**, 2003689 (2021).
[6] Y.-T. Liu, S. Liu, G.-R. Li, and X.-P. Gao, Strategy of enhancing the volumetric energy density for lithium–sulfur batteries, Adv. Mater. **33**, 2003955 (2021).
[7] J. He and A. Manthiram, A review on the status and challenges of electrocatalysts in lithium-sulfur batteries, Energy Stor. Mater. **20**, 55 (2019).
[8] M. Zhao, B.-Q. Li, H.-J. Peng, H. Yuan, J.-Y. Wei, and J.-Q. Huang, Lithium–sulfur batteries under lean electrolyte conditions: challenges and opportunities, Angew. Chem. Int. Ed. **59**, 12636 (2020).
[9] P. Wang, B. Xi, M. Huang, W. Chen, J. Feng, and S. Xiong, Emerging catalysts to promote kinetics of lithium–sulfur batteries, Adv. Energy Mater. **11**, 2002893 (2021).
[10] Q. Zhao, Q. Zhu, Y. Liu, and B. Xu, Status and prospects of mxene-based lithium–sulfur batteries, Adv. Funct. Mater. **31**, 2100457 (2021).
[11] Y. Liu, Y. Elias, J. Meng, D. Aurbach, R. Zou, D. Xia, and Q. Pang, Electrolyte solutions design for lithium-sulfur batteries, Joule **5**, 2323 (2021).
[12] W. Ren, W. Ma, S. Zhang, and B. Tang, Recent advances in shuttle effect inhibition for lithium sulfur batteries, Energy Stor. Mater. **23**, 707 (2019).
[13] Y. Zheng, S. Zheng, H. Xue, and H. Pang, Metal–organic frameworks for lithium–sulfur batteries, J. Mater. Chem. A **7**, 3469 (2019).
[14] X. Chen, T. Hou, K. A. Persson, and Q. Zhang, Combining theory and experiment in lithium–sulfur batteries: current progress and future perspectives, Mater. Today **22**, 142 (2019).
[15] R. Pai, A. Singh, M. H. Tang, and V. Kalra, Stabilization of gamma sulfur at room temperature to enable the use of carbonate electrolyte in Li-S batteries, Commun. Chem. **5**, 1 (2022).
[16] B. Zhang, J. Wu, J. Gu, S. Li, T. Yan, and X.-P. Gao, The fundamental understanding of lithium polysulfides in ether-based electrolyte for lithium–sulfur batteries, ACS Energy Lett. **6**, 537 (2021).
[17] O. Orcelus and A. A. Franco, Perspectives on manufacturing simulations of Li-S battery cathodes, J. Phys.: Energy **4**, 011002 (2022).
[18] J. B. Robinson, K. Xi, R. V. Kumar, A. C. Ferrari, H. Au, M.-M. Titirici, A. Parra-Puerto, A. Kucernak, S. D. Fitch, and N. Garcia-Araez, *et al.*, 2021 roadmap on lithium sulfur batteries, J. Phys.: Energy **3**, 031501 (2021).
[19] V. Ponce and J. M. Seminario, Lithiation of sulfur-graphene compounds using reactive force-field molecular dynamics simulations, J. Electrochem. Soc. **167**, 100555 (2020).
[20] P. Bhauriyal, S. Das, and B. Pathak, Theoretical insights into the charge and discharge processes in aluminum–sulfur batteries, J. Phys. Chem. C **124**, 11317 (2020).
[21] J. Zhu, P. Zhu, C. Yan, X. Dong, and X. Zhang, Recent progress in polymer materials for advanced lithium-sulfur batteries, Prog. Polym. Sci. **90**, 118 (2019).
[22] X. Zhang, K. Chen, Z. Sun, G. Hu, R. Xiao, H.-M. Cheng, and F. Li, Structure-related electrochemical performance of organosulfur compounds for lithium–sulfur batteries, Energy Environ. Sci. **13**, 1076 (2020).
[23] Q. Zhang, Q. Huang, S.-M. Hao, S. Deng, Q. He, Z. Lin, and Y. Yang, Polymers in lithium–sulfur batteries, Adv. Sci. **9**, 2103798 (2022).

[24] A. Hoefling, D. T. Nguyen, P. Partovi-Azar, D. Sebastiani, P. Theato, S.-W. Song, and Y. J. Lee, Mechanism for the stable performance of sulfur-copolymer cathode in lithium–sulfur battery studied by solid-state NMR spectroscopy, Chem. Mater. **30**, 2915 (2018).

[25] R. Kiani, D. Sebastiani, and P. Partovi-Azar, On the structure of sulfur/1,3-diisopropenylbenzene co-polymer cathodes for Li-S batteries: Insights from density-functional theory calculations, Chem. Phys. Chem. **23**, e202100519 (2022).

[26] T. N. L. Doan, M. Ghaznavi, Y. Zhao, Y. Zhang, A. Konarov, M. Sadhu, R. Tangirala, and P. Chen, Binding mechanism of sulfur and dehydrogenated polyacrylonitrile in sulfur/polymer composite cathode, J. Power Sources **241**, 61 (2013).

[27] J.-S. Kim, T. H. Hwang, B. G. Kim, J. Min, and J. W. Choi, A lithium-sulfur battery with a high areal energy density, Adv. Funct. Mater. **24**, 5359 (2014).

[28] A. Konarov, D. Gosselink, T. N. L. Doan, Y. Zhang, Y. Zhao, and P. Chen, Simple, scalable, and economical preparation of sulfur–PAN composite cathodes for Li/S batteries, J. Power Sources **259**, 183 (2014).

[29] J. Wang, J. Yang, J. Xie, and N. Xu, A novel conductive polymer–sulfur composite cathode material for rechargeable lithium batteries, Adv. Mater. **14**, 963 (2002).

[30] X. Yu, J. Xie, Y. Li, H. Huang, C. Lai, and K. Wang, Stable-cycle and high-capacity conductive sulfur-containing cathode materials for rechargeable lithium batteries, J. Power Sources **146**, 335 (2005).

[31] L. Wang, X. He, J. Li, M. Chen, J. Gao, and C. Jiang, Charge/discharge characteristics of sulfurized polyacrylonitrile composite with different sulfur content in carbonate based electrolyte for lithium batteries, Electrochim. Acta **72**, 114 (2012).

[32] S. S. Zhang, Understanding of sulfurized polyacrylonitrile for superior performance lithium/sulfur battery, Energies **7**, 4588 (2014).

[33] J. Wang, J. Yang, C. Wan, K. Du, J. Xie, and N. Xu, Sulfur composite cathode materials for rechargeable lithium batteries, Adv. Funct. Mater. **13**, 487 (2003).

[34] C.-J. Huang, J.-H. Cheng, W.-N. Su, P. Partovi-Azar, L.-Y. Kuo, M.-C. Tsai, M.-H. Lin, S. P. Jand, T.-S. Chan, and N.-L. Wu, *et al.*, Origin of shuttle-free sulfurized polyacrylonitrile in lithium-sulfur batteries, J. Power Sources **492**, 229508 (2021).

[35] V. Meunier, A. Souza Filho, E. Barros, and M. Dresselhaus, Physical properties of low-dimensional s p 2-based carbon nanostructures, Rev. Mod. Phys. **88**, 025005 (2016).

[36] L. Song, X. Zheng, R. Wang, and Z. Zeng, Dangling bond states, edge magnetism, and edge reconstruction in pristine and b/n-terminated zigzag graphene nanoribbons, J. Phys. Chem. C **114**, 12145 (2010).

[37] N. Gupta, V. I. Artyukhov, E. S. Penev, and B. I. Yakobson, Carbonization with misfusion: Fundamental limits of carbon-fiber strength revisited, Adv. Mater. **28**, 10317 (2016).

[38] L. Zhang, A. Aboagye, A. Kelkar, C. Lai, and H. Fong, A review: carbon nanofibers from electrospun polyacrylonitrile and their applications, J. Mater. Sci. **49**, 463 (2014).

[39] P. Partovi-Azar, S. P. Jand, and P. Kaghazchi, Electronic, Magnetic, and Transport Properties of Polyacrylonitrile-based Carbon Nanofibers of Various Widths: Density-Functional Theory Calculations, Phys. Rev. Appl. **9**, 014012 (2018).

[40] C. Tran, D. Lawrence, F. W. Richey, C. Dillard, Y. A. Elabd, and V. Kalra, Binder-free three-dimensional high energy density electrodes for ionic-liquid supercapacitors, Chem. Commun. **51**, 13760 (2015).

[41] M. K. Dufficy, S. A. Khan, and P. S. Fedkiw, Hierarchical graphene-containing carbon nanofibers for lithium-ion battery anodes, ACS Appl. Mater. Interfaces **8**, 1327 (2016).

[42] L. Wang, T. Mei, W. Liu, and Q. Zhou, A simple pyrolysis route to synthesize carbon nanofibers in molten zinc chloride as an anode material for Li ion batteries, J. Phys. Chem. C **120**, 5326 (2016).

[43] T. D. Kühne, M. Iannuzzi, M. Del Ben, V. V. Rybkin, P. Seewald, F. Stein, T. Laino, R. Z. Khaliullin, O. Schütt, and F. Schiffmann, *et al.*, Cp2k: An electronic structure and molecular dynamics software package-quickstep: Efficient and accurate electronic structure calculations, J. Chem. Phys. **152**, 194103 (2020).

[44] J. VandeVondele and J. Hutter, Gaussian basis sets for accurate calculations on molecular systems in gas and condensed phases, J. Chem. Phys. **127**, 114105 (2007).

[45] S. Goedecker, M. Teter, and J. Hutter, Separable dual-space Gaussian pseudopotentials, Phys. Rev. B **54**, 1703 (1996).

[46] J. P. Perdew, K. Burke, and M. Ernzerhof, Generalized Gradient Approximation Made Simple, Phys. Rev. Lett. **77**, 3865 (1996).

[47] S. Grimme, J. Antony, S. Ehrlich, and H. Krieg, A consistent and accurate ab initio parametrization of density functional dispersion correction (DFT-D) for the 94 elements H-PU, J. Chem. Phys. **132**, 154104 (2010).

[48] G. Bussi, D. Donadio, and M. Parrinello, Canonical sampling through velocity rescaling, J. Chem. Phys. **126**, 014101 (2007).

[49] J. M. Soler, E. Artacho, J. D. Gale, A. García, J. Junquera, P. Ordejón, and D. Sánchez-Portal, The SIESTA method for ab initio order-n materials simulation, J. Phys.: Condens. Matter **14**, 2745 (2002).

[50] N. Troullier and J. L. Martins, Efficient pseudopotentials for plane-wave calculations, Phys. Rev. B **43**, 1993 (1991).

[51] H. J. Monkhorst and J. D. Pack, Special points for Brillouin-zone integrations, Phys. Rev. B **13**, 5188 (1976).

[52] J. Martin, N. Akerman, G. Ulbricht, T. Lohmann, J. Smet, K. Von Klitzing, and A. Yacoby, Observation of electron–hole puddles in graphene using a scanning single-electron transistor, Nat. Phys. **4**, 144 (2008).

[53] Y. Zhang, V. W. Brar, C. Girit, A. Zettl, and M. F. Crommie, Origin of spatial charge inhomogeneity in graphene, Nat. Phys. **5**, 722 (2009).

[54] M. Gibertini, A. Tomadin, M. Polini, A. Fasolino, and M. Katsnelson, Electron density distribution and screening in rippled graphene sheets, Phys. Rev. B **81**, 125437 (2010).

[55] P. Partovi-Azar, N. Nafari, and M. R. R. Tabar, Interplay between geometrical structure and electronic properties in

rippled free-standing graphene, Phys. Rev. B **83**, 165434 (2011).

[56] Y. Schütze, R. de Oliveira Silva, J. Ning, J. Rappich, Y. Lu, V. G. Ruiz, A. Bande, and J. Dzubiella, Combined first-principles statistical mechanics approach to sulfur structure in organic cathode hosts for polymer based lithium–sulfur (Li–S) batteries, Phys. Chem. Chem. Phys. **23**, 26709 (2021).

[57] See Supplemental Material at http://link.aps.org/supplemental/10.1103/PhysRevApplied.18.044072 for remarks on reactant structures in lithiation reactions, stability of lithiated S/N-GNRs, magnetism in early discharge products, and sulfurized N-free GNRs.

[58] S. F. Boys and F. Bernardi, The calculation of small molecular interactions by the differences of separate total energies. Some procedures with reduced errors, Mol. Phys. **19**, 553 (1970).

[59] J. G. Speight, *Lange's Handbook of Chemistry* (McGraw-Hill Education, New York, 2017).

[60] T. Wassmann, A. P. Seitsonen, A. M. Saitta, M. Lazzeri, and F. Mauri, Structure, Stability, Edge States, and Aromaticity of Graphene Ribbons, Phys. Rev. Lett. **101**, 096402 (2008).